Korean J. Chem. Eng., 40(7), 1792-1803 (2023)
DOI: 10.1007/s11814-023-1347-9

pISSN: 0256-1115
eISSN: 1975-7220

A new class of M_x-$CuSb_2O_6$-$CuSb_2O_4$ (M_x=None, Fe, Ni, Ce and Yb) nanocomposites: Physical and electrochemical properties, and facile catalytic fabrication of 2-amino-4*H*-benzochromenes derivatives

Saideh Shafaati*, Alireza Hakimyfard*, Nemat Tahmasebi*,†, Leila Kafi-Ahmadi, and Shahin Khademinia*****

*Department of Physics, Faculty of Science, Jundi-Shapur University of Technology, Dezful, Iran
**Department of Inorganic Chemistry, Faculty of Chemistry, Urmia University, Urmia, Iran
***Department of Inorganic Chemistry, Faculty of Chemistry, Semnan University, Semnan, Iran
(*Received 18 October 2022 • Revised 22 December 2022 • Accepted 31 January 2023*)

Abstract−Solid state synthesis of some new M_x-$CuSb_2O_6$-$CuSb_2O_4$ (M_x=None, Fe, Ni, Ce and Yb) nanocomposites was introduced in the present research study. The physicoelectrochemical properties of synthesized nanocomposites were investigated by different techniques, such as XRPDT, Rietveld, FTIR, FESEM, UV-Vis, VSM, CV and EIS. Rietveld analysis data revealed that all of the synthesized samples display the monoclinic crystal phase with the space group of $P2_1/n$. The estimated direct band gap energy of the obtained nanocomposites was in the range of 2.0 to 2.7 eV, which confirms that are active in ultraviolet-visible region. The VSM data indicated that the maximum magnetic behavior was found for Ni doped - Cu-Sb-O nanocomposite. Also, the catalytic performance of nanocomposites to synthesis 2-amino-4*H*-benzochromenes under ultrasonic and microwave was investigated. The considered parameters, such as solvent type, catalyst amount and reaction time, influencing the yield of the 4*H*-benzochromene reaction were studied. The maximum yield for the synthesizing of the 4*H*-benzochromene compounds was obtained when EtOH was used as the reaction solvent. The catalyst amount and reaction time were 15 mol% and 8 min, respectively, under ultrasonic conditions, while benzaldehyde was used as an aldehyde derivative.

Keywords: $CuSb_2O_6$-$CuSb_2O_4$, Nanocomposite, Magnetic Property, Electrochemical Property, 2-Amino-4*H*-benzochromenes

INTRODUCTION

In the past decades, copper oxide as a p-type semiconductor has attracted much research attention due to its potentially application in antibacterial, gas sensing, magnetic and catalytic properties. The magnetic behavior of copper oxide is attributed to the unpaired electron of Cu^{2+} [1-4]. Magnetic Cu^{2+} ions are treated as spin-only and the effect of their unquenched orbital moment is included in an isotropic electron g tensor [5-8]. Examples of quasi-1D magnetism are found in materials that crystallize in the trirutile structure with chemical formula AB_2O_6 (A=magnetic, B=non-magnetic cations) [9-11]. $CuSb_2O_6$ is known to be a paramagnetic binary compound. $CuSb_2O_6$ is an exciting candidate exhibiting unusual magnetic behavior [12-14]. It crystallizes in monoclinically distorted trirutile structure type at room temperature. There are two polymorphs for $CuSb_2O_6$ including α-$CuSb_2O_6$ with tetragonal crystal system and the space group $P4_2/mnm$ with Z=2, lattice parameters of a=b= 4.63 Å, c=9.29 Å, and monoclinic crystal system with the space group $P2_1/n$ and unit cell parameters of a=4.6349 Å, b=4.6370 Å, c=9.2931 Å and β=91.124(2). The high-temperature α-$CuSb_2O_6$ phase shows slightly compressed CuO_6 octahedra along the 1D chain direction, while the β-$CuSb_2O_6$ phase shows elongated octahedral. Besides, $CuSb_2O_6$ grows in monoclinic crystal structure with the space group $P12_1/c1$ (14) and the lattice parameters of a=4.6200 Å, b=4.6200 Å, c=9.2800 Å and β=88.500° [15-18]. $CuSb_2O_4$ also crystallizes in a tetragonal crystal structure and space group of $P4_2bc$. with The fitted lattice parameters are a=b=8.7396(3) Å and c= 5.7853 Å, Z=4 [19-22]. Several works have reported synthesis of $CuSb_2O_6$ and $CuSb_2O_4$ nanomaterials, including solid state at 1,200 °C at 30 MPa pressure [23], solid state, using CuO and Sb_2O_3 at 1,000 °C [24], chemical vapor transport [25,26], flux method [27], solid state at 950 °C for 4 h using Sb_2O_3 and $CuSO_4$ [6], reflux [7,28], thermal decomposition of complexes [8], solid state at 900 °C for 24 h, then pelleting and 1,000 °C for 48 h [29], solid state at 1,000 °C under pure oxygen follow [15], solid state at 750 °C for 24 h and then 800 °C for 48 h [30], solid state at 950 °C for 12 h and then 1,000 °C for 12 h [19] and hydrothermal [31]. It is well known that the doping with metallic and nonmetallic elements is a traditional method to enhance the catalytic activity of semiconductor nanostructures. However, to date, only cobalt has been reported as dopant type for doping into $CuSb_2O_6$ or $CuSb_2O_4$ crystal systems [32]. Thus, in this work the effect of other dopants such as Fe, Ni, Ce and Yb on properties of $CuSb_2O_6$-$CuSb_2O_4$ composite has been investigated.

Chromene compounds are heterocycles main components of many naturally produced products. Chromene compounds are interesting because of their uses as cosmetic agents, food additives, and potential biodegradable agrochemicals. Also, chromene compounds show several pharmacological activities, including anti-HIV, anti-

†To whom correspondence should be addressed.
E-mail: tahmasebi@jsu.ac.ir

cancer, antileukemic, anticoagulant, diuretic, antibacterial, antitumor, antimalarial, antianaphylactic, and antimalarial applications. Also, chromene materials are components of various natural products like calophyllolides, calanolides, and calanone, the compounds are used in several diseases such as cognitive boosters for the cure of neurodegenerative diseases, such as Down syndrome, Parkinson's, Alzheimer's, etc. [33,34]. In the present study, microwave and ultrasonic conditions are used to synthesize the chromene derivatives. Microwave heating enhances the catalyst activity, where the polar reactant molecules have faster rotation rates and enter the transition state more rapidly than in a conventional heating system, resulting in increased reaction rates [35]. Ultrasonic irradiation on reaction mixture generates a huge number of cavitation bubbles that grow rapidly and subsequently undergo vigorous collapse, which results in the formation of micro-jets that can produce fine emulsion between the reactants [36].

The current experimental study describes the one-pot solid state synthesis of M_x-$CuSb_2O_6$-$CuSb_2O_4$ (M_x=None, Fe, Ni, Ce and Yb) nanocomposites. The physicoelectrochemical properties of synthesized nanocomposites were investigated by different techniques, such as XRPDT, FTIR, FESEM, UV-Vis, VSM, CV and EIS. The main crystal phase and space group types were determined by refinement of the XRPD patterns by Rietveld analysis. Besides, the efficiency and performance of the samples for the production of 2-amino-4*H*-benzochromene derivatives were focused. The novelties of the present work are synthesis of a new class of M_x-Cu-Sb-O mixed metal oxides by solid state method, introducing the synthesized samples as capacitor confirmed by EIS and CV analysis. Also, excellent catalytic performance of the M_x-Cu-Sb-O nanocomposites for chromene reactions is introduced for the first time in the present work.

EXPERIMENTAL

1. Materials and Methods

All reagents used in this work were pure and purchased from commercial Sigma Aldrich company. The materials were applied without any re-purification. The crystal structure of synthesized materials was characterized by powder X-ray diffraction (XRD) technique (Siemens D5000, Germany) with CuK_α radiation. Field emission scanning electron microscopy (FESEM) was applied to investigate the morphology and elemental analysis of samples (Philips XL30, Netherlands) The investigation of the optical properties to estimate the band gap energy of samples involved a UV-visible spectrophotometer (Shimadzu-UV-1650 PC, Japan). Fourier-transform infrared spectroscopy (FTIR) spectra of the samples were investigated by a Tensor 27 spectrometer (Bruker Corporation, Germany). A vibrating sampling magnetometer was applied to study the magnetic assets of the nanocomposites (VSM-7400-LakeShore). The heating of the reaction combination was carried out using an oil bathtub. Microwave irradiation was done at 1,000 W by a Yusch Heating Microwave oven.

2. Solid State Synthesis of M_x-$CuSb_2O_6$-$CuSb_2O_4$ (M_x=None, Fe, Ni, Ce and Yb) Nanocomposites

M_x-$CuSb_2O_6$-$CuSb_2O_4$ (M_x=None, Fe, Ni, Ce and Yb) nanocomposites were produced by mixing 0.21 g (1.0 mmol) of $CuCl_2$ (Mw=211.62 g mol^{-1}) and 0.15 g (1.0 mmol) of Sb_2O_3 (Mw=197.87 g mol^{-1}). After the powders were ground together in a mortar, the mixed homogeneous powder which had been transferred to a 25 mL crucible was annealed in an electrical furnace at 800 °C for 8 h [S_1] and 1,000 °C for 10 h [S_2] under normal atmosphere. To synthesize the doped nanocomposites, the synthesis procedure was done according to S_2 using 0.01 mmol of $Fe(NO_3)_3{\cdot}9H_2O$ (MW=404 $gmol^{-1}$) [S_3], $Ni(NO_3)_2{\cdot}6H_2O$ (MW=290.8 $gmol^{-1}$) [S_4], $Ce(NO_3)_3{\cdot}6H_2O$ (MW=434.2 $gmol^{-1}$) [S_5] and Yb_2O_3 (MW=394.1 $gmole^{-1}$) [S_6]. In a typical experiment, 0.10 g of $CuCl_2$, 0.15 g (1.0 mmol) of Sb_2O_3 and 0.01 mmole of $Fe(NO_3)_3$ were mixed together, ground and heated at 1,000 °C for 10 h. After the reaction was completed at the desired condition, the furnace was turned off and the samples normally reached room temperature.

3. General Remarks for Fabricating 2-Amino-4*H*-chromene Compounds

To investigate the catalytic activity of nanocomposites under microwave illumination, malononitrile (**2**, 1 mmol), aromatic aldehydes (1, 1 mmol), β-naphthol (**3**, 1 mmol) and nanocatalyst (15 mol%) were mixed in a 5 mL solvent and put in a microwave oven. The reaction mixture was illuminated by microwave irradiation for a particular time (for example, 12 min) until the reaction was done. The final touch of the reaction was acknowledged with the assistance of thin layer chromatography (TLC) (n-Hexane : Ethyl acetate 6 : 4). When the reaction was completed, hot ethanol (10 mL) was added into the reaction solution to dissolve the product. To separate the catalyst layer, the alcoholic mixture was poured onto a Buchner funnel covered by a Whatman filter paper until the satisfactory solution was passed and the catalyst was marinated on the filter paper. Chromene products were recovered by the alcohol evaporation and then recrystallized from ethanol.

4. Working Electrode Fabrication for Electrochemical Properties

In this work, the working electrode was fabricated by the missing of graphite powder, silicon oil and $CuSb_2O_4$-$CuSb_2O_6$ nanocomposite in the ratio of 10 : 80 : 10 (w/w). In each experiment, the mixture was homogeneously combined in a mortar, and the final paste was tightly packed into a glass tube to eliminate air content. A copper wire was inserted through the center of one side of the paste packed glass tube without any crack to make the electrical contact. After a run for the electrochemical test, the side that was in contact with the electrolyte solution was polished mechanically using a butter sheet to renew and shine the surface of the working electrode.

RESULTS AND DISCUSSION

1. Characterization

Figs. 1(a)-(d) and 2(A)-(D) represent the XRPD patterns of the as-fabricated nanocomposites. Rietveld analysis data confirmed the production of the described samples. The red dots are the observed intensities, while the black lines are the calculated data by the Rietveld analysis. The Bragg reflection positions are indicated by green bars, which correspond to the crystal phases. The blue line under the green bars is the difference between the observed and calculated data: $Y_{obs}-Y_{calc}$. The data shown in Fig. 1(a) reveals that

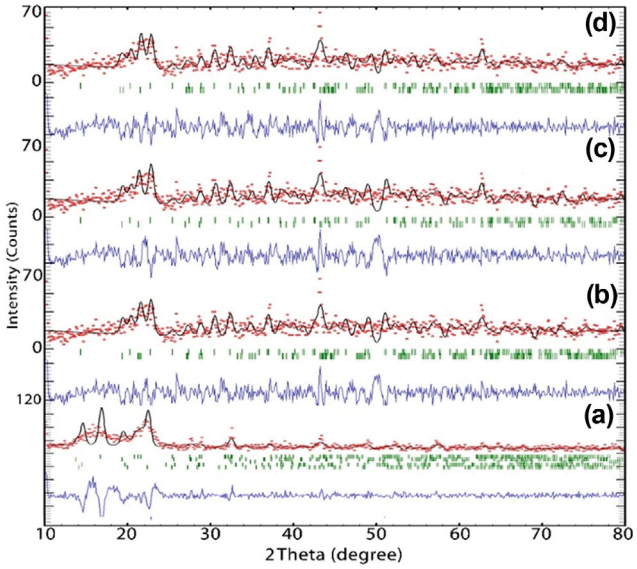

Fig. 1. XRPD patterns and the Rietveld refinement data of (a) S_1, (b), (c) and (d) S_2 with the space group of (b) $P2_1/n$, (c) $P12_1c1$ and (d) $P4_2/mnm$ space groups.

the compounds are mixtures of $CuSb_2O_4$ and $CuSb_2O_6$ crystal phases. However, it seems that the crystalline nature of the compound is not so good, and broad peaks with low intensity are observed. So, the higher reaction temperature was used to synthesize the target. It was found that the XRD peak intensity of the materials was increased when the reaction temperature was increased. Fig. 1(b)-(d) presents a comparison among the reported space groups in which $CuSb_2O_6$ can be crystallized. Table 2 presents Rietveld refinements parameters values for the fabricated samples when the three different space groups are used in the refinement process. The values of χ^2, for S_2, representing the goodness of Rietveld analysis refinement are 1.59, 1.78 and 2.60, respectively, for $P2_1/n$, (b) $P12_1c1$, and (c) $P4_2/mnm$ space groups. The data show that the preference of the space group can be $P2_1/n$. The data shown in Table 2 reveal that the analysis of the XRPD patterns with $P4_2/mnm$ resulted in a bad refinement. However, the refinement with $P2_1/n$ and $P12_1/c1$ showed similar behavior and no considerable difference was found in same cell parameter values conditions. The Miller indices for the main peaks of $CuSb_2O_6$ with $P12_1/c1$ space group are 20.07° (110), 35.05 (013), and 38.72 (220). The Miller indices for the main peaks of $CuSb_2O_4$ with $P12_1/c1$ space group are 27.46° (211), 38.60 (212), 52.33 (402), and 53.44 (412).

Lattice volume (V) was calculated by the below formula for the monoclinic crystal phase system:

$$V = a.b.c.\sin(\beta)$$

The D values of the as-fabricated compounds were measured by

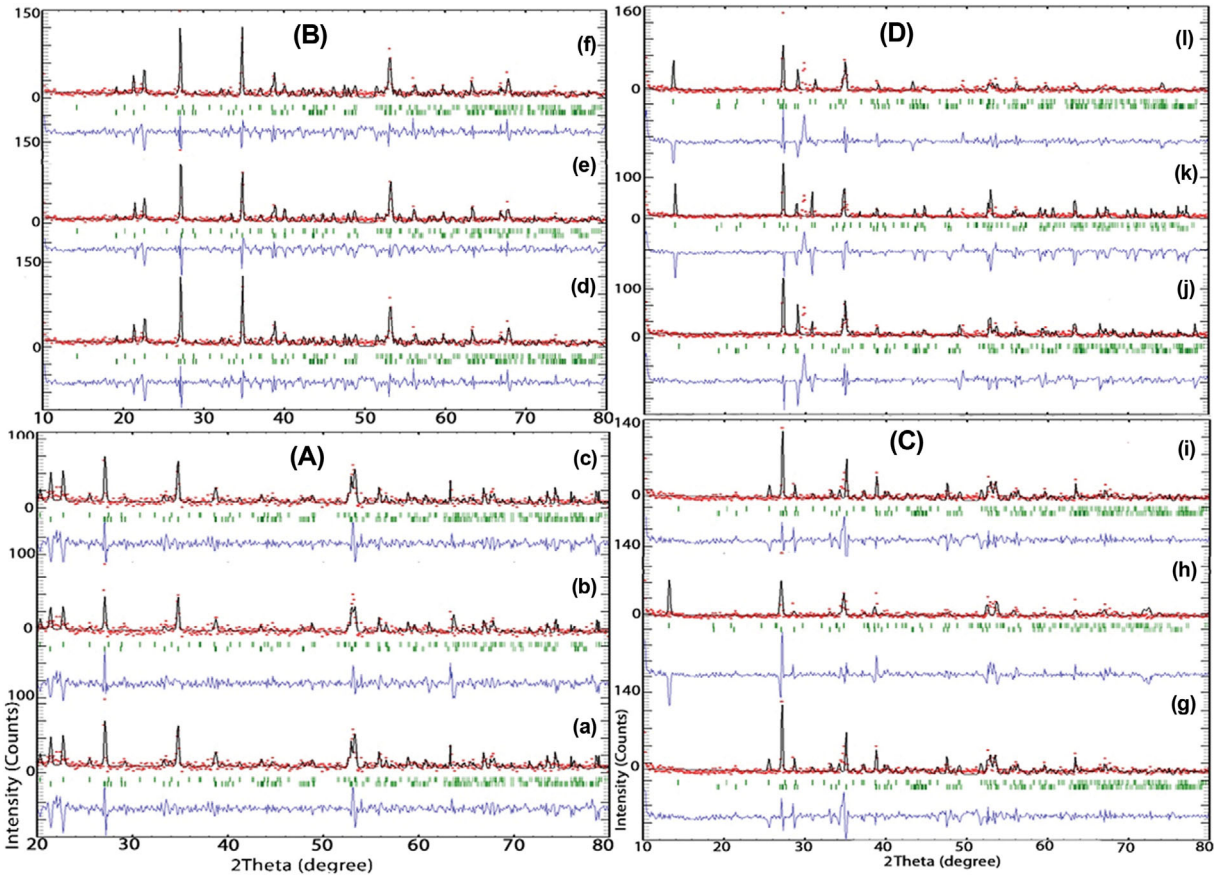

Fig. 2. XRPD patterns and the Rietveld analysis data of (A) S_3, (B) S_4, (C) S_5 and (D) S_6 in which (a), (d), (g), (j) $P2_1/n$, (b), (e), (h), (k) $P12_1c1$ and (c), (f), (i), (l) $P4_2/mnm$ space groups.

Table 1. Unit cell, crystallite size (D), dislocation density (δ), strain (ε), X-ray density (ρ_x), specific surface area (SSA), $CuSb_2O_4$/$CuSb_2O_6$ crystal phase ratio and counts data of the synthesized $CuSb_2O_6$ nanocomposites

	2θ	$B_{1/2}$	a	b	c	V (Å^3)	β	D	$\delta\times10^{-3}$	d (Å)	ρ_x	SSA	$\varepsilon\times10^{-3}$	$CuSb_2O_4$ ratio	Counts
S_1	43.2	0.015	4.51	4.68	9.74	205	91.27	13	5.9	2.23	0.59	7.8	2.6	1.3	75
S_2	43.3	0.007	4.61	4.69	9.35	202	91.12	21	6.6	2.07	0.66	4.3	2.8	1.5	76
S_3	27.2	0.004	4.52	4.68	9.40	199	91.12	34	2.4	3.25	0.67	2.6	1.7	0.6	87
S_4	27.3	0.003	4.61	4.66	9.28	199	91.15	44	2.4	3.27	0.67	2.0	1.7	0.7	149
S_5	27.3	0.003	4.68	4.63	9.32	202	91.19	44	2.4	3.27	0.66	2.0	1.7	0.4	128
S_6	27.2	0.003	4.66	4.64	9.28	201	91.12	44	2.4	3.27	0.67	2.0	1.7	0.4	148

Table 2. Rietveld refinement parameters values for the synthesized samples

Parameters	$P2_1/n$			$P4_2/mnm$			$P12_1c1$		
	R_F	R_{Bragg}	χ^2	R_F	R_{Bragg}	χ^2	R_F	R_{Bragg}	χ^2
S_1	1.93	2.93	2.47	3.56	4.73	2.30	2.98	3.31	3.26
S_2	0.534	1.08	1.59	1.39	2.77	2.60	0.93	1.21	1.78
S_3	1.68	1.94	1.54	3.73	3.83	1.84	1.73	2.01	1.68
S_4	1.31	2.48	1.61	2.31	3.48	1.61	1.18	2.76	1.66
S_5	1.24	2.27	1.93	4.94	6.17	2.97	1.64	2.40	2.18
S_6	1.72	2.99	2.07	6.42	9.61	1.96	1.45	2.45	2.22

Scherrer equation using the data obtained by Rietveld analysis (Table 1):

$$D=\frac{K\lambda}{B_{1/2}\cos\theta}$$

Dislocation density (δ) parameter value is calculated by the below formula:

$$\delta=\frac{1}{D^2}$$

The value of strain (ε) parameter is from the below equation:

$$\varepsilon=\frac{\beta_{hkl}\cos\theta}{4}$$

The strain value decreases by purity increasing of the crystal nature that is caused by the crystallite degree improving of the fabricated compounds. Table 1 presents the calculated data indicating the influence of the reaction temperature and doping on the D, δ, and ε values.

To calculate the d values, we used the Bragg equation and compared the obtained data with the d value calculated by the following equation:

$$\frac{1}{d^2}=\frac{1}{\sin^2\beta}\left(\frac{k^2\sin^2\beta}{b^2}+\frac{l^2}{c^2}-\frac{2hl\cos\beta}{ac}\right)$$

The 2θ and β values are included in Table 1. The (hkl) value for S_1 and S_2 is (-202), and for S_3-S_6 is (012) and =91.12°, respectively, for the monoclinic crystal system. It is known that sin (91.12)=0.9998 and cos (91.30)=−0.0195.

$$\frac{1}{d^2}=\left(\frac{4}{c^2}+\frac{8}{ac}\right)$$

for S_1 and S_2, and

$$\frac{1}{d^2}=\left(\frac{1}{b^2}+\frac{4}{c^2}\right)$$

for S_3-S_6.

The X-ray density (ρ_x) value included in Table 1 is calculated by the below formula:

$$\rho_x=\frac{ZM}{Na.b.c}$$

In the formula, the molecular weight of $CuSb_2O_6$ (M_W=403 gmol^{-1}) is defined by M, the Avogadro number is defined by N, formula unit number per lattice for α-$CuSb_2O_6$ (Z=2) is defined by Z, and the lattice parameter is defined by a, b, c. The calculated values for ρ_x reveal that the ρ_x values are small and do not show considerable change by changing the conditions of the synthesis reactions and/or introducing the metal ions into the host crystal system. Besides, as can be found from the data, it shows that no observable change caused by the intercalation of the metal ions, with various atomic weight and density, is found when the synthesis reaction conditions are changed.

The specific surface area (SSA) per lattice volume is a compound property affecting the physical, chemical, and photochemical efficiency/properties. The parameter SSA is obtained by measuring ρ_{xrd} and grain size (D) by the below equation:

$$SSA=\frac{6{,}000}{D\rho_{xrd}}$$

2. Morphology Analysis

FESEM images of the as-produced S_1 to S_6 nanocomposites, respectively, are shown in Fig. 3a-f. As can be found from Fig. 3a, the morphology of the S_1 is particle. The particle size of the sample is about 20-30 nm. It is found that the other compounds' morphology is particle. However, the particles are in the range of micron

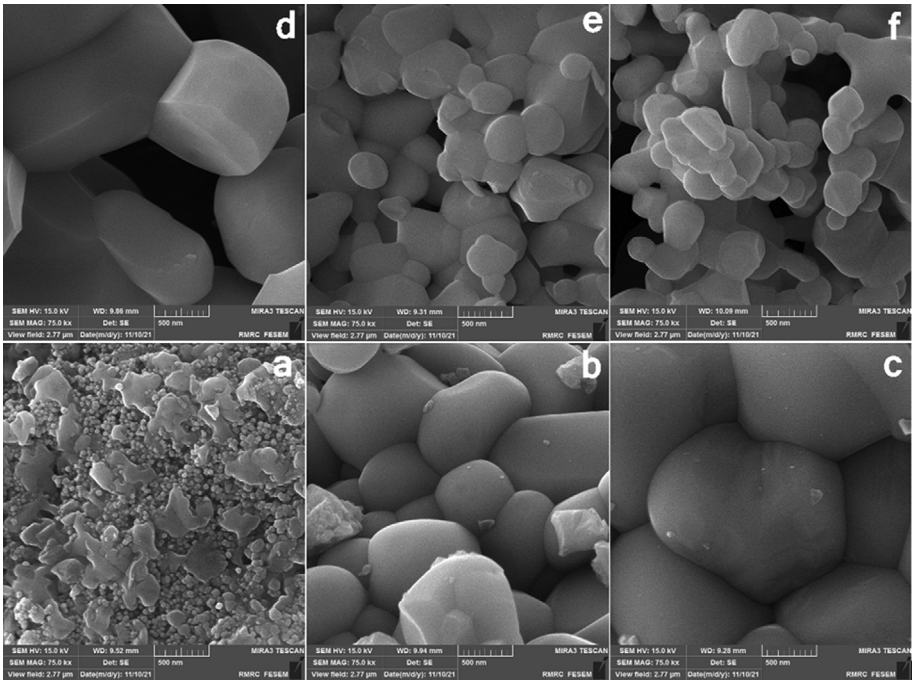

Fig. 3. FESEM images of a) S_1, b) S_2, c) S_3, d) S_4, e) S_5 and f) S_6.

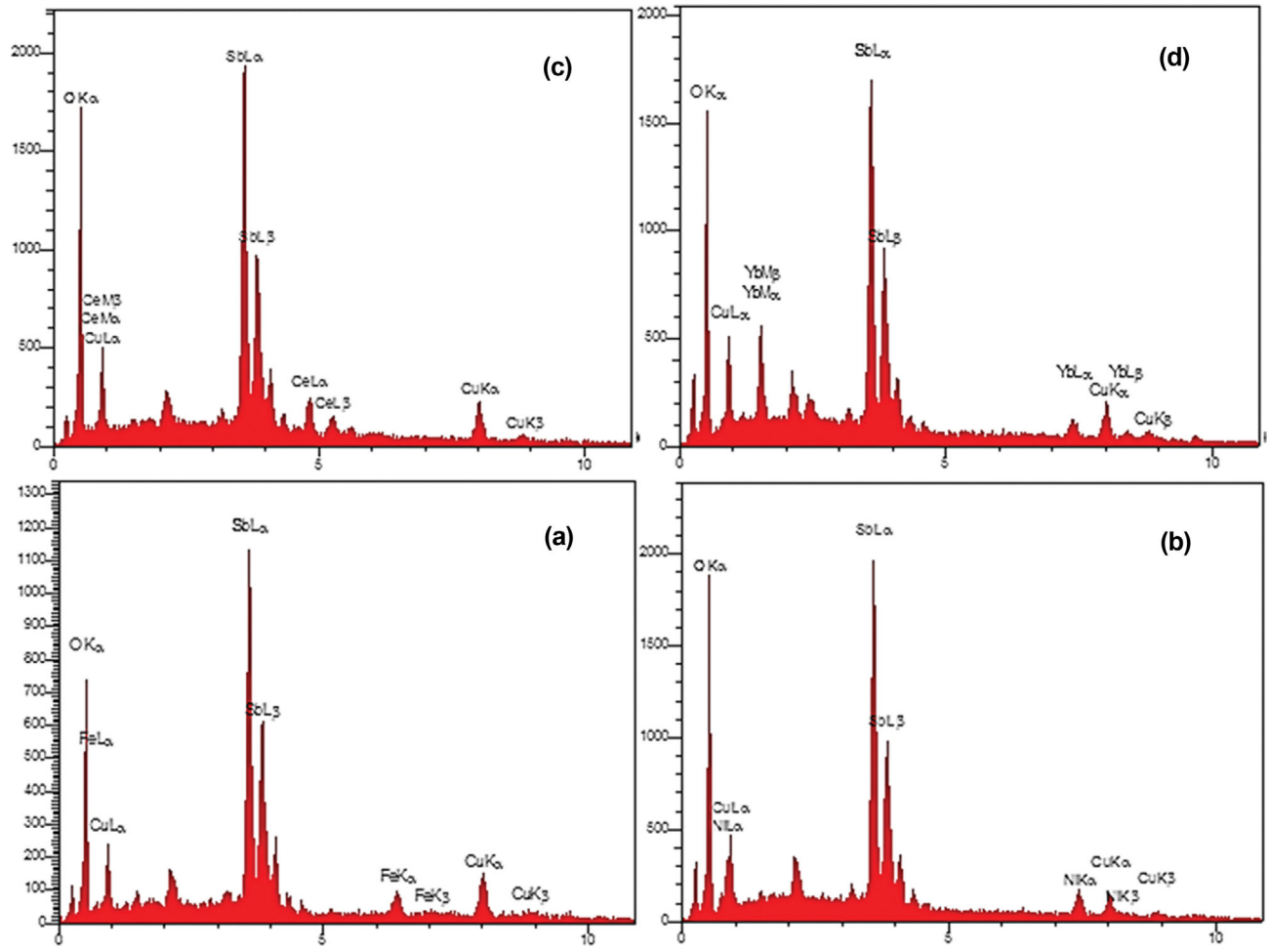

Fig. 4. EDX graphs of (a) S_3, (b) S_4, (c) S_5, and (d) S_6.

size. Besides, it is found that the particles are in multigonal shape. The particle sizes are in the ranges of 250 nm to 1 μm.

3. Elemental Analysis

As shown in Fig. 4, to determine the amount of the dopant into the samples, EDX technique was applied. According to the analysis, the intercalation percent (A%) of Fe^{3+}, Ni^{2+}, Ce^{3+} and Yb^{3+} in the composites was 0.013, 0.016, 0.011, and 0.012, respectively.

4. Magnetic Properties

VSM analysis was used to investigate the magnetic behavior of the as-fabricated compounds. As shown in Fig. 5(a) and (b), the magnetic hysteresis (M-H) curves of the as-produced nanocomposites display ferromagnetic property at 273 K. According to Fig. 5(a), the saturation magnetization (M_s) amount changes from 0.05 to 0.20 emu/g. The M_s amount increases by introducing Ni^{2+} into the host crystal system (S_4). Remanence magnetization, M_r, parameter is defined by magnetization strength of a compound, where the magnetization is not eliminated by eliminating the external magnetic field (H=0) [37]. Fig. 5(b) shows the magnified M-H curve. It shows that S_1 has the most saturation remanence (M_r) values (0.014). M_s value for S_1 is 0.1 emu/g. The squareness ratio (M_{rs}=M_r/M_s) value is obtained by the dividing the remanence by saturation magnetization. A compound has a squareness ratio smaller than 0.5 when the magnetization distribution of a particle is isotropical and uniform without intergrain interactions. The observation is related to the formation of multi-domain structure. In the current experimental study, it is shown that M_{rs} is 0.14 for S_1. So, no preferred magnetization direction is observed for the as-fabricated compounds.

5. Optical Properties

Fig. 6(a) and (d) show the UV-Vis absorption and the direct optical band gap energy graphs of the as-produced nanocomposites. According to Fig. 6(a), the absorption of light in the ultraviolet-visible region suggests fantastic photoactivity under ultraviolet and visible light irradiations. The absorption coefficient and the energy of the incident wavelength are related together by $(\alpha h\nu)^2=A(h\nu-E_g)$ for E_g, where, A and E_g are constant and direct band gap energy value, respectively. The extrapolation of the linear part of the curve to the energy axis is considered as E_g value. It can be seen from Fig. 6(b) that the band gap energies of pure and doped samples are in the range of 2.05-2.9 eV. This figure indicates that the S6

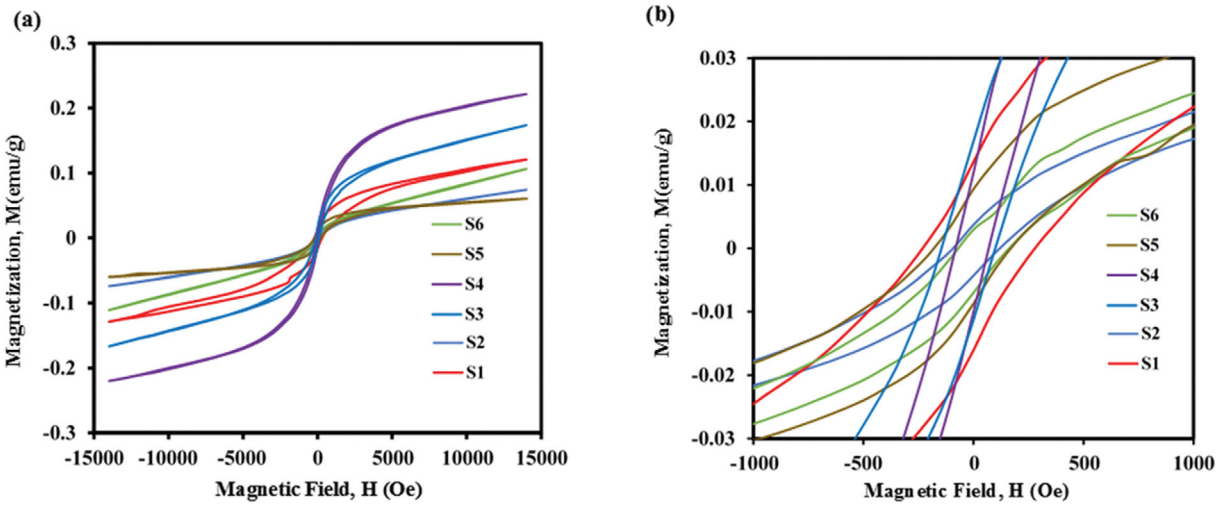

Fig. 5. Room temperature M-H graphs of the as-fabricated nanocomposites.

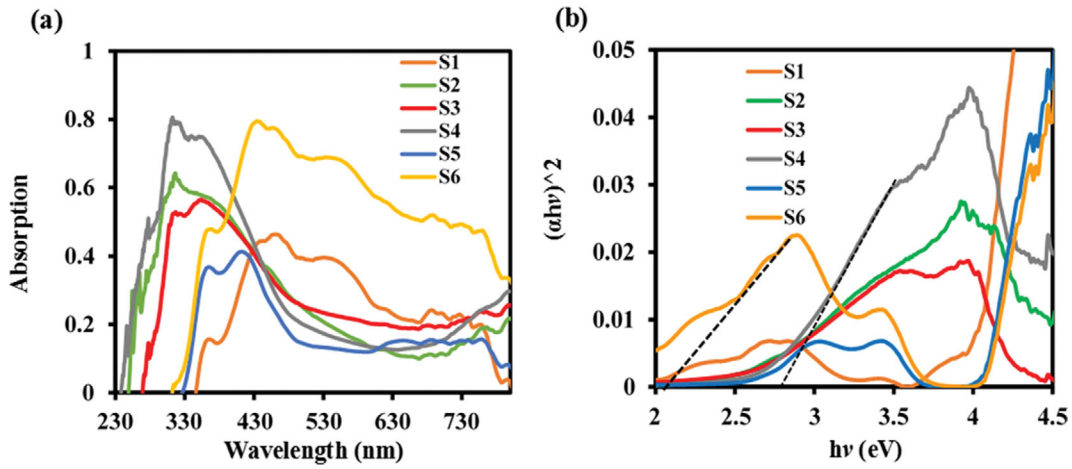

Fig. 6. (a) UV-Vis spectra and (b) direct band gap energy values of the as-produced compounds.

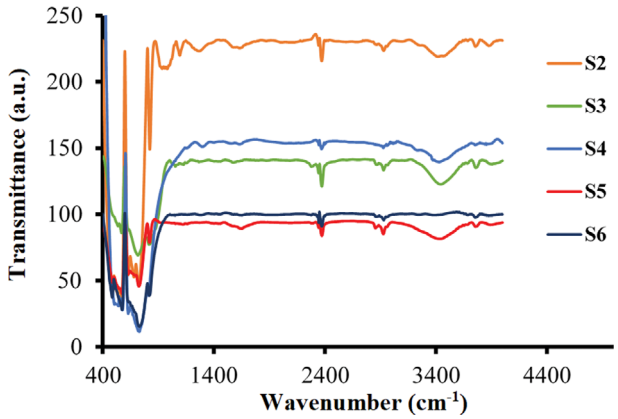

Fig. 7. FTIR spectra of the as-produced nanocomposites.

sample displays the smallest E_g with the value of 2.7 eV. However, the previously reported E_g value for the pure $CuSb_2O_6$ was 3.3 eV [8]. The decrease in the value of the band gap energy can be due to the composite nature of the as-prepared samples.

FTIR spectra of the as-produced nanocomposites are shown in Fig. 7. The main bands are centered at 580, 735, 820, 2,370 and 3,460 cm^{-1}. The band at 580 cm^{-1} is related to symmetric bending vibration of Sb-O [38]. The band at 735 cm^{-1} is assigned to Cu-O-Sb vibration [39]. The band at 820 cm^{-1} is also attributed to Sb-O stretching vibration. The broad band at about 3,460 cm^{-1} was assigned to stretching vibration of the O-H bonds [40].

6. Electrochemical Properties

An electrochemical system composed of a three-electrode cell including working electrode, reference electrode, and counter electrode was used to study the electrochemical property of the as-produced nanocomposites by cyclic voltammetry (CV). The galvanostatic charge/discharge measurement (V-t curves) at a stable current intensity is presented in Fig. 8a showing a symmetric triangular shape revealing no considerable iR loss. The observation indicates a good capacitive behavior of the compound. So, the data shows that the nanocomposite is useful for making capacitor electrode. The voltage-time plot of the as-produced compounds indicates an ideal linear figure and no deviation is found for the compound. So, no quick faradaic reaction caused by the existence of excess oxygen-containing functional groups was found [41]. But, when the scan rate increases, the charge/discharge time is reduced. The electrochemical impedance spectroscopy (EIS) graph of the as-fabricated compounds is presented in Fig. 8b and c. The data related the overall conductivity of the cell and its impact on the power and the discharge behavior of the sample. As could be found from the data, it is clear that the Z values are about 25 to 60 Ω/cm^2 for the synthesized samples. It is clear that the smallest value belongs to S_5. The area of semicircle region for S_5 is less than that of the other samples. The observation is due to the higher electron and charge transfer rate for S_5. Weak ion and electron transport results from the relatively observed high EIS values of the capacitors. Besides,

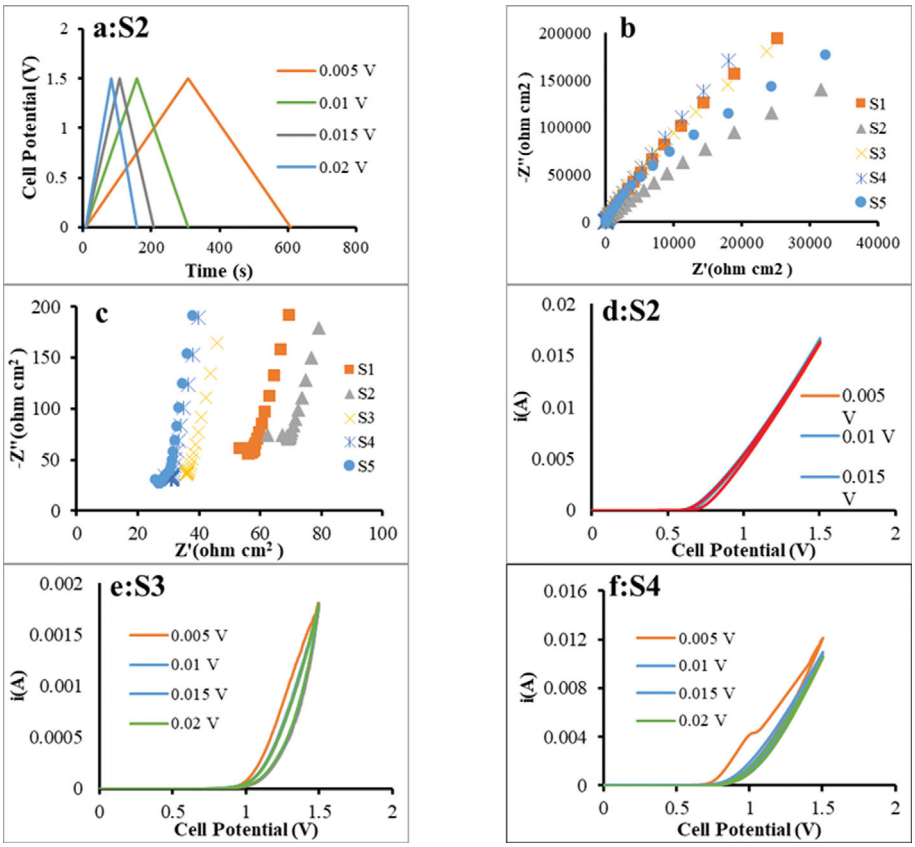

Fig. 8. a) galvanostatic charge–discharge, b, c) Nyquist, d-h') CV, and i) i-t plots of the as-produced nanocomposites.

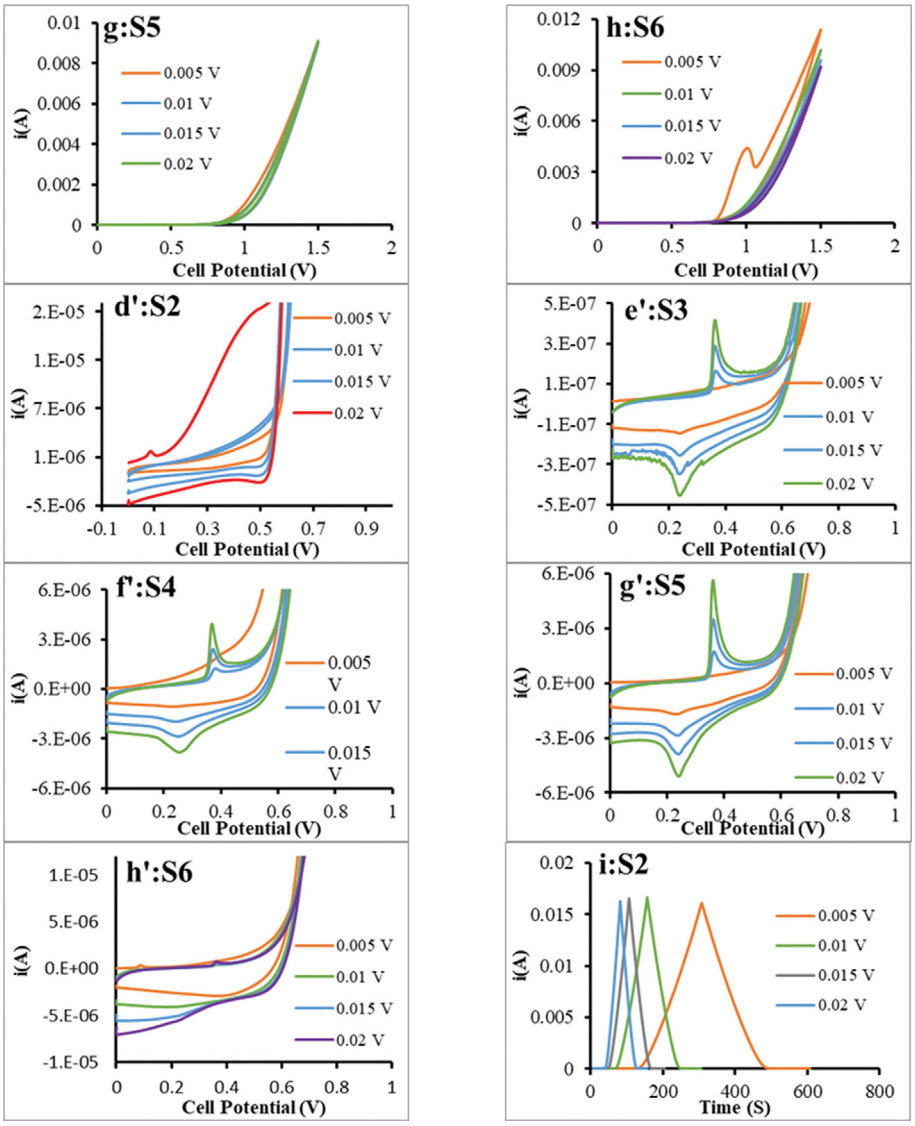

Fig. 8. Continued.

the graphs slopes are near to 90° showing the good capacitor property of the samples, which is in agreement with the CV results [42].

Fig. 8d-h presents the cyclic voltammograms of the as-produced compounds in 1 molL^{-1} NaOH aqueous solution between 0 and +1.5 V at different scan rates. The CV curves of the nanocomposites do not show a typical rectangular shape. This phenomenon confirms that there no capacitive behavior is caused by pure electric double layer and oxidation-reduction reactions for the working electrode at the cell potential range. The electrochemical window (EW) is defined for materials in which no oxidation-reduction reaction is observed in a certain cell potential range. The magnified CV graphs shown in Fig. 8f-h indicate that the compounds have wide potential windows, and so the nanocomposites are stable against oxidation/reduction reaction. Aans c be seen from the plots, the data indicate that the current density values are in the ranges of 0 to +0.6, 0 to 0.9, 0 to 0.70, 0 to 0.8 and 0 to 0.8 V, respectively, for S_2, S_3, S_4, S_5 and S_6. Besides, a weak broad shape at about 0 V reveals a small pseudocapacitive property of the compounds. The observations show that the samples present a good onset potential and more current density in the CV curve, implying a larger capacitance when the dopant types are intercalated into the host crystal system [43]. As can be found from Fig. 8d-h, the magnified plots show that the samples suffer a very small oxidation-reduction reaction at the potential range. It shows that the samples can be used as electrocatalyst applications. The i-t curve is shown in Fig. 8i; it shows that the peaks exist at the lower time when the scan rate increases.

The charge discharge specific capacitance is calculated by the below equation [44]:

$$C = \frac{i \times dt}{m(V_f - V_i)}$$

In the equation, the applied current is i, the discharging time is dt, the mass of the active material coated on to the electrode is m, and the working potential window is (V_f–V_i). In the present experimental study, m is 0.01 g and i is 0.05 A/cm^2. The dt (s) values are 172,

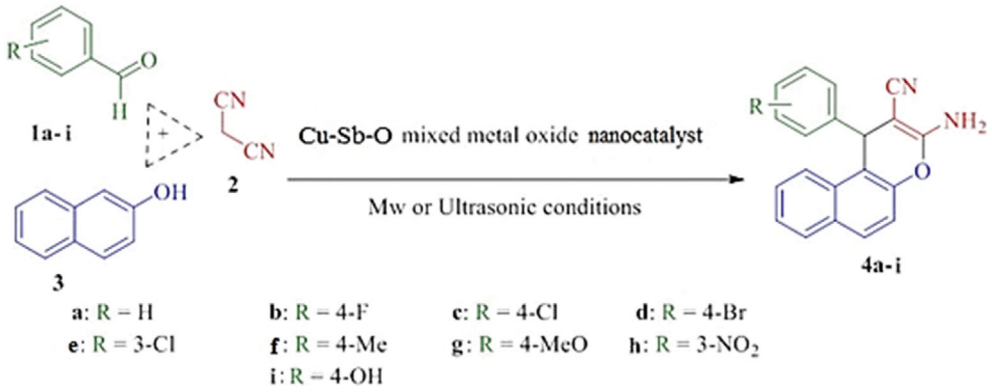

Scheme 1. Catalytic reaction route for the fabrication of 2-amino-4*H*-benzochromenes by Cu-Sb-O nanostructure.

89, 48 and 47, respectively, for 0.005, 0.01, 0.015 and 0.02 V/s scan rates.

7. Catalytic Study

The fabrication of 2-amino-4*H*-benzochromenes under ultrasonic and microwave conditions by the as-prepared nanocomposite (S_2) is presented in the current work. Some reaction parameters affecting the chromene manufacturing yield, which includes reaction time, catalyst quantity, and solvent kind, have been studied to obtain an excessive yield. Scheme 1 shows the standard reaction way for the fabricating of the chromene compounds below microwave illumination. The reaction yield was 98% when R=H and EtOH as a solvent, at 45 °C for 8 min by using 15 mol% catalyst.

The reaction time, solvent type, temperature, and catalyst amount, in different reaction conditions including microwave and ultrasonic, are studied in Tables 3-6, respectively. The data presented in Table 3 show that the maximum reaction yield of 98% was obtained under ultrasonic conditions when the radiation frequency, temperature and reaction time were 50 (kHz), 45 °C and 8 min, respectively.

Table 3. Influence of the temperature and the reaction time on the reaction yield of the typical reaction

Temperature (°C)	Frequency (KHz)	Time (min)	Yield (%)
	Ultrasonic		
25	10	18	80
30	20	15	83
35	30	12	87
40	40	10	90
45	50	8	98
50	60	8	93
	Microwave		
Temperature (°C)	M.W power (W)	Time (min)	Yield (%)
30	40	22	71
35	50	17	79
40	60	13	85
45	70	9	90
50	80	5	97
55	90	5	92

benzaldehyde (1 mmol), *β*-naphthol (1 mmol), malononitril (1 mmol) and 15 mol% of catalyst (S_1) in EtOH.

Besides, when the microwave power, time, and temperature were 80 W, 5 min, and 50 °C, 97% yield was obtained. Additionally, the impact of solvent type on the 4*H*-benzochromene reaction yield is presented in Table 4. The observation shows that the maximum reaction yield is achieved when EtOH is used as the reaction solvent. As could be found from the Table, the time amount to reach the maximum yield for each reaction condition is different. However, the reaction yield is about zero when solvent-free condition is applied. The catalyst amount effect on the reaction yield was also studied in Table 5. It was found that a high yield was obtained when 15 mol% of S_2 was used in the reaction mixture.

The catalytic reaction yields with the melting point of the recrystallized compounds using S_2 as catalyst are presented in Table 6.

Table 4. Influence of the solvent on the reaction time and yield of the typical reaction

Entry	Solvent	Time (min)	Yield (%)
	Ultrasound		
1	-	120	-
2	H_2O	20	64
3	EtOH	8	98
4	H_2O/EtOH(1 : 1)	16	83
5	H_2O/EtOH(1 : 2)	13	88
6	CH_2Cl_2	26	45
7	DMF	28	50
8	$(C_2H_5)_2O$	25	42
9	CH_3CN	26	49
	Microwave		
1	-	44	23
2	H_2O	17	55
3	EtOH	5	97
4	H_2O/EtOH(1 : 1)	13	60
5	H_2O/EtOH(1 : 2)	10	62
6	CH_2Cl_2	22	46
7	DMF	20	50
8	$(C_2H_5)_2O$	24	45
9	CH_3CN	20	49

benzaldehyde (1 mmol), *β*-naphthol (1 mmol), malononitril (1 mmol) and 15 mol% of catalyst (S_1) in 50 °C and 80 W microwave power.

Table 5. Influence of the catalyst amount on reaction yield of the typical reaction

Entry	Catalyst (mol%)	Time (min)	Yield (%)
	Ultrasound		
1	-	30	9
2	5	22	54
3	10	16	73
4	15	8	98
5	20	6	94
	Microwave		
1	-	20	66
2	5	9	90
3	10	7	94
4	15	5	97
5	20	5	95

benzaldehyde (1 mmol), β-naphthol (1 mmol), malononitril (1 mmol) and various amount of catalyst (S_1) in EtOH, 50 °C and 80 W microwave power.

The values included in Table 6 confirm that the most catalyst efficiency was obtained when the reaction time was lower than 10 min, for ultrasonic and microwave conditions.

Tables 7 and 8 present the catalytic efficiency of the as-prepared samples for the Chromene reactions at the optimum conditions under ultrasonic and microwave conditions. As could be found from the data, it was found that the catalytic efficiency of the samples under the two conditions is comparable. However, it is clear that a bit weak in the efficiency of the catalysts is found when doped samples were used in the reaction mixture. The FTIR and NMR data are included in the supplementary file.

8. Reusability of Catalyst

The reusability test of the applied catalyst in the Chromene reaction mixture was studied under microwave condition. According to the data, considerable reaction yield was obtained until run=3. The deactivation of the catalyst after run 3 can be due to the saturation of the active sites of the catalyst by organic compounds and/or decomposition of the catalyst after three times of the catalytic process. The XRD pattern of the catalyst after three times reactions is also shown in Fig. 9(b). It is clear that the count value of the catalyst has decreased considerably. Also, the proportion of $CuSb_2O_4$ in the product mixture has decreased. According to the data we can conclude that the main reason for the decrease of the catalyst performance is decomposition and reducing the crystalline nature of the catalyst. The data are demonstrated by the refs. [45,56].

Table 9 presents the comparison study for the catalytic synthesis of Chromene compounds. As could be found from the data, it is clear that the efficiency of the as-prepared nanocomposites for the present catalytic reaction is comparable with the other reported works.

Table 6. Production of 2-amino-4*H*-benzochromenes under microwave and ultrasound irradiation

Entry	Aldehyde	Product	Microwave conditions[a]		Ultrasonic conditions[b]	
			Time (min)	Yield (%)	Time (min)	Yield (%)
1	C_6H_5CHO	4a	5	97	8	98
2	4-FC_6H_4CHO	4b	7	94	6	96
3	4-ClC_6H_4CHO	4c	6	96	6	95
4	4-BrC_6H_4CHO	4d	7	95	7	96
5	3-ClC_6H_4CHO	4e	6	94	7	94
6	4-MeC_6H_4CHO	4f	9	92	8	93
7	4-$OMeC_6H_4CHO$	4g	7	90	10	89
8	3-$NO_2C_6H_4CHO$	4h	4	98	4	98
9	4-OHC_6H_4CHO	4i	10	89	9	90

[a]Aldehyde derivatives (1 mmol), malononitrile (1 mmol), β-naphthol (1 mmol) and catalyst (S_1) 15 mol% in EtOH and power of 80 W in 50 °C.
[b]Aldehyde derivatives (1 mmol), malononitrile (1 mmol), β-naphthol (1 mmol) and catalyst (S_1) 15 mol% in EtOH and 50 kHz frequency in 45 °C.

Table 7. Catalytic performance of S_1, S_3, S_4, S_5 and S_6 at the optimum conditions under microwave illumination

Entry	Aldehyde	Product	Y(%) S_1	Y(%) S_3	Y(%) S_4	Y(%) S_5	Y(%) S_6
1	C_6H_5CHO	4a	95	94	92	93	93
2	4-FC_6H_4CHO	4b	93	91	90	89	90
3	4-ClC_6H_4CHO	4c	94	92	91	90	91
4	4-BrC_6H_4CHO	4d	93	91	90	89	90
5	3-ClC_6H_4CHO	4e	93	92	91	91	90
6	4-MeC_6H_4CHO	4f	91	90	88	89	89
7	4-$OMeC_6H_4CHO$	4g	88	87	86	86	85
8	3-$NO_2C_6H_4CHO$	4h	97	95	94	93	94
9	4-OHC_6H_4CHO	4i	87	86	85	84	84

Table 8. Catalytic activity of S_1, S_3, S_4, S_5 and S_6 at the optimized conditions under ultrasonic conditions

Entry	Aldehyde	Product	Y(%) S_1	Y(%) S_3	Y(%) S_4	Y(%) S_5	Y(%) S_6
1	C_6H_5CHO	4a	97	96	94	95	95
2	4-FC_6H_4CHO	4b	95	93	92	91	92
3	4-ClC_6H_4CHO	4c	93	91	90	89	89
4	4-BrC_6H_4CHO	4d	95	94	93	92	91
5	3-ClC_6H_4CHO	4e	93	93	92	90	91
6	4-MeC_6H_4CHO	4f	92	91	90	88	89
7	4-$OMeC_6H_4CHO$	4g	87	85	84	83	83
8	3-$NO_2C_6H_4CHO$	4h	97	96	95	94	95
9	4-OHC_6H_4CHO	4i	89	88	86	87	85

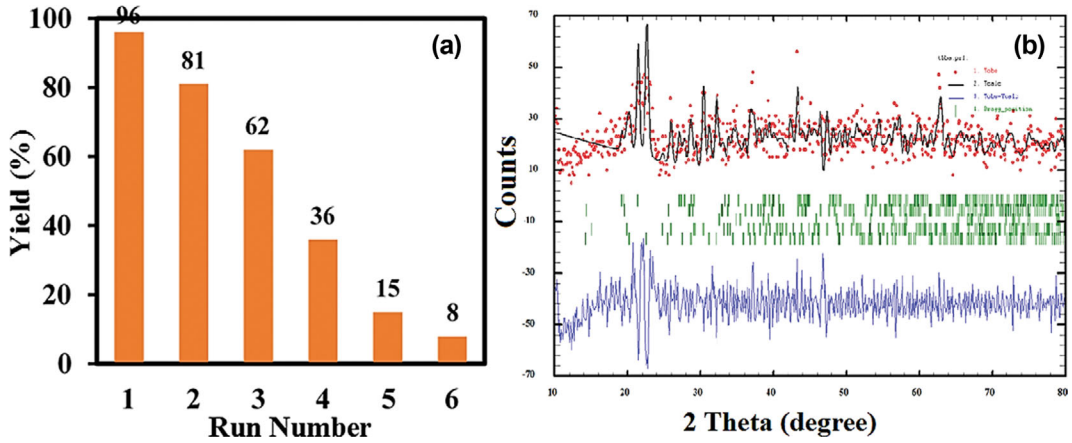

Fig. 9. (a) Reusability efficiency and (b) XRD pattern of S_2 for the Chromene reaction under microwave illumination.

Table 9. Comparison study for the catalytic fabrication of Chromene derivatives

Entry	Sample	Yield	Ref.
1	$CuSb_2O_4$-$CuSb_2O_6$	97	Present work
2	Pd@Graphene	94	[47]
3	ZnO	95	[48]
4	ZnO-Al_2O_3	81	[49]
5	Fe_3O_4@SiO_2	96	[50]
6	$Ag_2Cr_2O_7$	96	[51]

CONCLUSION

A facile solid state procedure was used to prepare M_x-$CuSb_2O_6$-$CuSb_2O_4$ (M_x=None, Fe, Ni, Ce and Yb) nanocomposites. The physicoelectrochemical properties of synthesized nanocomposites were investigated by different techniques, such as XRPDT, Rietveld, FTIR, FESEM, UV-Vis, VSM, CV and EIS. The UV-Vis data indicated that the Yb-doped $CuSb_2O_6$-$CuSb_2O_4$ sample exhibited the smallest band gap energy with the energy of 2.7 eV. Besides, the VSM data confirmed that the highest magnetic property was found for Ni-doped $CuSb_2O_6$-$CuSb_2O_4$ nanocomposite. CV data revealed that the synthesized samples had capacitor behavior; however, a very weak electrochemical active oxidation/reduction reaction was observed. Cu-Sb-O nanocomposites were used as a reusable nanocatalyst for the synthesis of 2-amino-4*H*-chromenes under ultrasonic and microwave illumination. The maximum yield for the preparation of the 2-amino-4*H*-benzochromenes was obtained at 97% when H_2O was used as the reaction solvent; the catalyst amount, reaction time and temperature, and illumination frequency were 15 mol%, 12 min, 70 °C, and 50 kHz, respectively, while benzaldehyde was used as aldehyde derivative.

SUPPORTING INFORMATION

Additional information as noted in the text. This information is available via the Internet at http://www.springer.com/chemistry/journal/11814.

REFERENCES

1. O. Scarlat, A. C. Payne, S. Mihaiu, G. Aldica and M. Zaharescu, *J. Optoelectron. Adv. Mater.*, **5**, 997 (2003).
2. A. Rebello, M. G. Smith, J. J. Neumeier, B. D. White and Y.-K. Yu, *Phys. Rev. B*, **87**, 224427 (2013).
3. A. B. Christian, S. H. Masunaga, A. T. Schye, A. Rebello, J. J. Neumeier and Y.-K. Yu, *Phys. Rev. B*, **90**, 224423 (2014).
4. N. Prasai, A. Rebello, A. B. Christian, J. J. Neumeier and J. L. Cohn, *Phys. Rev. B*, **91**, 054403 (2015).
5. M. T. Atanasova, A. M. Strydom, C. J. H. Schutte, L. C. Prinsloo and W. W. Focke, *J. Mater Sci.*, **49**, 3497 (2014).

6. A. Yu. Nikulin, E. A. Zvereva, V. B. Nalbandyan, I. L. Shukaev, A. I. Kurbakov, M. D. Kuchugura, G. V. Raganyan, Yu. V. Popov, V. D. Ivanchenko and A. N. Vasiliev, *Dalton Trans.*, **46**, 6059 (2017).
7. M. T. Atanasova, A. M. Strydom, C. J. H. Schutte, L. C. Prinsloo and W. W. Focke, *J. Mater. Sci.*, **49**, 3497 (2014).
8. S. Atri, S. Uma and R. Nagarajan, *Mater. Sci. Semicond. Process.*, **119**, 105226 (2020).
9. E.-O. Giere, A. Brahimi, H. J. Deiseroth and D. Reinen, *J. Solid State Chem.*, **131**, 263 (1997).
10. A. Rebello, M. G. Smith, J. J. Neumeier, B. D. White and Y.-K. Yu, *Phys. Rev. B: Condens. Matter.*, **87**, 224427 (2013).
11. A. M. Nakua and J. E. Greedan, *J. Solid State Chem.*, **118**, 199 (1995).
12. D. Kasinathan, K. Koepernik and H. Rosner, *Phys. Rev. Lett.*, **100**, 237202 (2008).
13. M. Kato, A. Hatazaki, K. Yoshimura and K. Kosuge, *Phys. B*, **281**, 663 (2000).
14. M. Herak, D. Žilić, D. Matković-Calogović and H. Berger, *Phys. Rev. B: Condens. Matter.*, **91**, 174436 (2015).
15. E.-O. Giere, A. Brahimi, H. J. Deiseroth and D. Reinen, *J. Solid State Chem.*, **131**, 263 (1997).
16. D. T. Maimone, A. B. Christian, J. J. Neumeier and E. Granado, *Phys. Rev. B*, **97**, 104304 (2018).
17. S. Simada and K. J. D. Mackenzie, *Thermochim. Acta*, **56**, 73 (1982).
18. A. Nakua, H. Yun, J. N. Reimers, J. E. Greedan and C. V. Stager, *J. Solid State Chem.*, **91**, 105 (1991).
19. E. I. Ramos, J. Isasi, M. Galtan and M. L. Veiga, *An. R. Soc. Esp. Quím.*, **87**, 966 (1991).
20. S. Shimada, K. Kodaira snd T. Matsushita, *J. Solid State Chem.*, **59**, 237 (1985).
21. S. Shimada, K. J. D Mackenzie, K. Kodaira, T. Matsushita and T. Ishii, *Thermochim. Acta*, **133**, 73 (1988).
22. E. O. Giere, A. Brahimi, H. J. Deiseroth and D. Reinen, *J. Solid State Chem.*, **131**, 263 (1997).
23. M. Zaharescu, S. Mihaiu, S. Zuca and K. Matiasovsky, *J. Mater. Sci.*, **26**, 1666 (1991).
24. A. Nakua, H. Yun, J. N. Reimers, J. E. Greedan and C. V. Stager, *J. Solid State Chem.*, **91**, 105 (1991).
25. A. Rebello, M. G. Smith, J. J. Neumeier, B. D. White and Y.-K. Yu, *Phys. Rev. B*, **87**, 224427 (2013).
26. A. V. Prokofiev, F. Ritter, W. Assmus, B. J. Gibson and R. K. Kremer, *J. Crystal Growth*, **247**, 457 (2003).
27. S. Shimada, K. Kodaira and T. Matsushita, *J. Crystal Growth*, **72**, 753 (1985).
28. W. W. Focke, S. S. Mkhize, R. Storey, O. D. Fabbro and E. Muller, *Chem. Eng. Comm.*, **201**, 153 (2014).
29. K. Kato, K. Kajimoto, K. Yoshimura, K. Kosuge, M. Nishi and K. Kakurai, *J. Phys. Soc. Jpn.*, **71**, 187 (2002).
30. M. Kato, Y. Nogi, S. Hongo and K. Hirota, *J. Phys.: Conference Series*, **344**, 012010 (2012).
31. S. Jiao, G. Pang, H. Liang, Y. Chen and S. Feng, *J. Nanopart. Res.*, **9**, 605 (2007).
32. H.-B. Kang, C. D. Ling and T. Söhnel, Proceedings – 38th Annual Condensed Matter and Materials Meeting – Waiheke Island, Auckland, NZ (2014).
33. H. A. Oskooie, M. M. Heravi, N. Karimi and G. Kohansal, *Synth. Commun.*, **41**, 2763 (2011).
34. N. Lukasik and E. W. Wysiecka, *Curr. Org. Syn.*, 11 (2014).
35. D. Muley, Y. Wang, J. Hu and D. Shekhawat, *Catalysis*, **33**, 1 (2021).
36. B. Banerjee, *Ultrason. Sonochem.*, **35**, 1 (2017).
37. M. Parishani, M. Nadafan, Z. Dehghani, R. Malekfar and G. H. H. Khorrami, *Results. Phys.*, **7**, 3619 (2017).
38. S. Y. Marzouk and F. H. Elbatal, *J. Mol. Struct.*, **1063**, 328 (2014).
39. O. Scarlat, M. Susana-Mihaiu and M. Zaharescu, *J. Eur. Ceram. Soc.*, **22**, 1839 (2002).
40. W. Tang, L. Liu, S. Tian, L. Li, Y. Yue, Y. Wu and K. Zhu, *Chem. Commun.*, **47**, 10058 (2011).
41. W. Chen, J. Zhao, Y. Li, S. Li, C. Jin, C. Yang, X. Feng, J. Zhang and L. Mi, *Chem. Electro. Chem.*, **1**, 601 (2014).
42. Y. Li, X. Feng, S. Cui, Q. Shi, L. Mi and W. Chen, *Cryst. Eng. Comm.*, 1 (2013).
43. P. Connor, J. Schuch, B. Kaiser and W. Jaegermann, Z. *Phys. Chem.*, **234**, 979 (2020).
44. C. R. Ravikumar, M. R. Anil Kumar, H. P. Nagaswarupa, S. C. Prashantha, A. S. Bhatt, M. S. Santosh and D. Kuznetsov, *J. Alloy. Compd.*, **738**, 332 (2018).
45. Y. Yang, K. Jiang, J. Guo, J. Li, X. Peng, B. Hong, X. Wang and H. Ge, *Chem. Eng. J.*, **381**, 122596 (2020).
46. X.-Q. Zhang, R.-F. Shen, X.-J. Guo, X. Yan, Y. Chen, J.-T. Hu and W.-Z. Lang, *Chem. Eng. J.*, **408**, 128018 (2021).
47. S. Akocak, B. Şen, N. Lolak, A. Şavk, M. Koca, S. Kuzu and F. Şen, *Nano-Struct. Nano-Objects*, **11**, 25 (2017).
48. S. Zavar, *Arab. J. Chem.*, **10**, 67 (2017).
49. B. N. Mahato, T. Krithiga, J. A. Kumar and G. Yogalakshmi, *Can. J. Chem.*, **100** (2022).
50. R. E. Keihan, S. Bahrami, M. G. Gorab, Z. Sadat and A. Maleki, *Sci. Rep.*, **12**, 10664 (2022).
51. M. Ebrahimi, S. Abdolmohammadi and R. K. Kojoori, *Polycycl. Aromat. Compd.*, **42**, 3440 (2022).

Supporting Information

A new class of M_x-$CuSb_2O_6$-$CuSb_2O_4$ (M_x=None, Fe, Ni, Ce and Yb) nanocomposites: Physical and electrochemical properties, and facile catalytic fabrication of 2-amino-4*H*-benzochromenes derivatives

Saideh Shafaati*, Alireza Hakimyfard*, Nemat Tahmasebi*,†, Leila Kafi-Ahmadi, and Shahin Khademinia*****

*Department of Physics, Faculty of Science, Jundi-Shapur University of Technology, Dezful, Iran
**Department of Inorganic Chemistry, Faculty of Chemistry, Urmia University, Urmia, Iran
***Department of Inorganic Chemistry, Faculty of Chemistry, Semnan University, Semnan, Iran
(*Received 18 October 2022 • Revised 22 December 2022 • Accepted 31 January 2023*)

FTIR and NMR Spectroscopies Analyses

The FTIR and ^{1}H-NMR spectroscopies analyses data of compounds **4a-i** are given below:

3-Amino-1-phenyl-1*H*-benzo[*f*]chromene-2-carbonitrile (Entry 1):

White solid; M.p.(Obsd.) 285-288 °C; M.p.(Lit.). 285-287 °C; IR (KBr, v, cm^{-1}): 3,451, 3,351, 2,179, 1,669, 1,600, 1,540, 1,501, 1,190, 1,081; ^{1}H NMR (DMSO-d_6): δ 7.93-7.82 (m, 2H, Ar), 7.85 (d, *J*= 6.1 Hz, 1H, Ar), 7.44-7.15 (m, 8H, Ar), 6.93 (bs, 2H, NH_2), 5.30 (s, 1H, CH); CHN ($C_{20}H_{14}N_2O$) calc. (%): C (80.53), H (4.69), N (9.39); observed (%): C (80.21), H (4.50), N (9.02).

3-Amino-1-(4-fluorophenyl)-1*H*-benzo[*f*]chromene-2-carbonitrile (Entry 2):

Light yellow solid; M.p. 237-240 °C; M.p.(Lit.). 239-241 °C; IR (KBr, v, cm^{-1}): 3,405, 3,339, 2,191, 1,632, 1,572, 1,400, 1,256, 1,109, 1,033, 804, 757; ^{1}H NMR (DMSO-d_6): δ 7.91-7.89 (m, 2H, Ar), 7.87-7.80 (m, 1H, Ar), 7.44 (d, *J*=6.1 Hz, 2H, Ar), 7.32-7.21 (m, 2H, Ar), 7.19 (d, *J*=8.5 Hz, 1H, Ar), 7.04 (t, 2H, Ar), 6.95 (bs, 2H, NH_2), 5.28 (s, 1H, CH); CHN ($C_{20}H_{13}FN_2O$) calc. (%): C (75.94), H (4.11), N (8.86); observed (%): C (75.42), H (4.08), N (8.29).

3-Amino-1-(4-chlorophenyl)-1*H*-benzo[*f*]chromene-2-carbonitrile (Entry 3):

White solid; M.p. 211-213 °C; M.p.(Lit.). 210-212 °C; IR (KBr, v, cm^{-1}): 3,408, 3,332, 2,190, 1,640, 1,572, 1,408, 1,248, 1,100, 1,044, 801, 755; ^{1}H NMR (DMSO-d_6): δ 7.85 (d, *J*=8.0 Hz, 1H, Ar), 7.47 (d, *J*=8.2 Hz, 1H, Ar), 7.43-7.28 (m, 3H, Ar), 7.15 (d, *J*=8.1 Hz, 2H, Ar), 6.94 (d, *J*=8.5 Hz, 2H, Ar), 7.10 (d, *J*=8.3 Hz, 1H, Ar), 7.01 (bs, 2H, NH_2), 5.30 (s, 1H, CH); CHN ($C_{20}H_{13}ClN_2O$) calc. (%): C (72.18), H (3.90), N (8.42); observed (%): C (71.89), H (3.56), N (8.14).

3-Amino-1-(4-bromophenyl)-1*H*-benzo[*f*]chromene-2-carbonitrile (Entry 4):

White solid; M.p. 219-221 °C; M.p.(Lit.). 220-222 °C; IR (KBr, v, cm^{-1}): 3,400, 3,333, 2,192, 1,647, 1,570, 1,401, 1,256, 1,107, 1,052, 800, 769; ^{1}H NMR (DMSO-d_6): δ 7.90-7.83 (m, 2H, Ar), 7.75-7.70 (m, 1H, Ar), 7.46-7.39 (m, 3H, Ar), 7.33-7.26 (m, 1H, Ar), 7.24-7.11 (m, 2H, Ar), 7.10 (d, *J*=8.1 Hz, 1H, Ar), 7.00 (bs, 2H, NH_2), 5.28 (s, 1H, CH); CHN ($C_{20}H_{13}BrN_2O$) calc. (%): C (63.67), H (3.44), N (7.42); observed (%): C (63.32), H (3.17), N (7.20).

3-Amino-1-(3-chlorophenyl)-1*H*-benzo[*f*]chromene-2-carbonitrile (Entry 5):

White solid; M.p. 210-212 °C; M.p.(Lit.). 211-213 °C; IR (KBr, v, cm^{-1}): 3,437, 3,350, 2,179, 1,656, 1,600, 1,562, 1,518, 1,500, 1,317, 1,270, 1,060, 765; ^{1}HNMR (DMSO-d_6): δ 8.00 (s, 1H, Ar), 7.96 (d, *J*=8.1 Hz, 1H, Ar), 7.94 (d, *J*=7.5 Hz, 1H, Ar), 7.90 (d, *J*=7.0 Hz, 1H, Ar), 7.82 (d, *J*=8.0 Hz, 1H, Ar), 7.53 (d, *J*=7.6 Hz, 1H, Ar), 7.50-7.47 (m, 1H, Ar), 7.40-7.45 (m, 2H, Ar), 7.33 (d, *J*=8.0 Hz, 1H, Ar), 7.10 (bs, 2H, NH_2), 5.66 (s, 1H, CH); CHN ($C_{20}H_{13}ClN_2O$) calc. (%): C (72.18), H (3.90), N (8.42); observed (%): C (72.09), H (3.54), N (8.21).

3-Amino-1-(*p*-tolyl)-1*H*-benzo[*f*]chromene-2-carbonitrile (Entry 6):

White solid; M.p. 268-270 °C, M.p.(Lit.). 269-271 °C; IR (KBr, v, cm^{-1}): 3,440, 3,320, 2,946, 2,166, 1,662, 1,607, 1,526, 1,499, 1,262, 1,175, 1,069, 744; ^{1}H NMR (DMSO-d_6): δ 7.90 (d, *J*=7.1 Hz, 2H, Ar), 7.88-7.80 (m, 1H, Ar), 7.40 (d, *J*=7.6 Hz, 2H, Ar), 7.28 (d, *J*= 8.2 Hz, 1H, Ar), 7.26-7.11 (m, 4H, Ar), 6.85 (bs, 2H, NH_2), 5.17 (s, 1H, CH), 2.15 (s, 3H, CH_3); CHN ($C_{21}H_{16}N_2O$) calc. (%): C (80.76), H (5.12), N (8.97); observed (%): C (80.39), H (4.88), N (8.57).

3-Amino-1-(4-methoxyphenyl)-1*H*-benzo[*f*]chromene-2-carbonitrile (Entry 7):

Pale yellow solid; M.p. 189-191 °C; M.p.(Lit.). 191-193 °C; IR (KBr, v, cm^{-1}): 3,422, 3,318, 2,975, 2,170, 1,664, 1,600, 1,525, 1,509, 1,293, 1,230, 1,180, 1,075, 762; ^{1}H NMR (DMSO-d_6): δ 7.87 (d, *J*=8.1 Hz, 2H, Ar), 7.60 (t, *J*=7.1 Hz, 1H, Ar), 7.32-7.21 (m, 2H, Ar), 7.13 (d, *J*=8.0 Hz, 1H, Ar), 7.01 (d, *J*=8.0 Hz, 2H, Ar), 6.88 (d, *J*=8.3 Hz, 2H, Ar), 6.80 (bs, 2H, NH_2), 5.20 (s, 1H, CH), 3.59 (s, 3H, OCH_3); CHN ($C_{21}H_{16}N_2O_2$) calc. (%): C (76.82), H (4.87), N (8.53); observed (%): C (76.44), H (4.39), N (8.22).

3-Amino-1-(3-nitrophenyl)-1*H*-benzo[*f*]chromene-2-carbonitrile (Entry 8):

White solid; M.p. 231-233 °C; M.p.(Lit.). 233-235 °C ; IR (KBr, v, cm^{-1}): 3,444, 3,350, 2,182, 1,666, 1,607, 1,579, 1,520, 1,500, 1,322, 1,271, 1,063, 760; ^{1}HNMR (DMSO-d_6): δ 8.00 (s, 1H, Ar), 7.89 (d, *J*=8.0 Hz, 1H, Ar), 7.90 (d, *J*=7.2 Hz, 1H, Ar), 7.86 (d, *J*=7.5 Hz, 1H, Ar), 7.74 (d, *J*=8.4 Hz, 1H, ArH), 7.54 (d, *J*=7.6 Hz, 1H, Ar), 7.50-7.41 (m, 1H, Ar), 7.38-7.30 (m, 2H, Ar), 7.26 (d, *J*=8.0 Hz, 1H, Ar), 7.05 (bs, 2H, NH_2), 5.66 (s, 1H, CH); CHN ($C_{20}H_{13}N_3O_3$)

calc. (%): C (69.97), H (3.79), N (12.24); observed (%): C (69.43), H (3.21), N (12.07).

3-Amino-1-(4-hydroxyphenyl)-1*H*-benzo[*f*]chromene-2-carbonitrile (Entry 9):

White solid; M.p. 287-289 °C; M.p.(Lit.). 289-291 °C; IR (KBr, v, cm^{-1}): 3,440, 3,352, 2,186, 1,669, 1,601, 1,579, 1,522, 1,500, 1,327, 1,271, 1,060, 764; ^{1}HNMR (DMSO-d_6): δ 7.93-7.90 (m, 2H, ArH), 7.89-7.83 (m, 1H, Ar), 7.40 (d, J=6.0 Hz, 2H, Ar), 7.37-7.20 (m, 2H, Ar), 7.19 (d, J=8.6 Hz, 1H, Ar), 7.08 (t, 2H, Ar), 7.00 (bs, 2H, NH_2), 5.40 (s, 1H, CH), 10.20 (s, 1H, OH), CHN ($C_{20}H_{14}N_2O_2$) calc. (%): C (76.43), H (4.45), N (8.91); observed (%): C (76.22), H (4.08), N (8.33).